

Torque Capacity Improvement of Flux-Switching PM Machines Based on Directional Stator Permeance Design

Hong Chen, *Member, IEEE*, Dawei Li, *Senior Member, IEEE*,
and Ronghai Qu, *Fellow, IEEE*, and Tianjie Zou, *Member, IEEE*

Abstract—As one type of flux modulation machines, flux-switching permanent magnet (FSPM) machines present high sensitivity to airgap structures. Therefore, both stator/rotor teeth and slot/pole combinations have significant influences on machine performance. However, the relationships between the optimal stator structure and maximum torque capability of the FSPM machine are barely investigated. Therefore, this paper is devoted to proposing a directional stator permeance design approach to achieve the maximum torque of the FSPM machines under a given rotor, and reveal the corresponding stator structure. First, the relations between torque and air-gap permeance are presented based on a constructed torque contribution equation, where amplitudes and phase angles of the stator permeance harmonics are determined. Then, main permeance harmonics are directionally optimized to enlarge positive torque, while negative contributions are inverted to be positive. Especially, two FSPMs with 6-slot/19-pole and 6-slot/13-pole are chosen as design examples, and their optimal design processes and torque performances have been deeply analyzed, which verifies the effectiveness of the proposed design approach.

Index Terms—Flux-switching permanent magnet (FSPM) machine, permeance harmonic design, stator structure, torque capacity.

I. INTRODUCTION

CONVENTIONAL flux-switching permanent magnet (FSPM) machine is normally equipped with a segmented stator, fractional slot concentrated windings (FSCWs), stationary spoke-PMs, and a robust salient rotor. [1]. Hence, the FSPM machines can achieve good thermal management and high-speed operation without magnet retention. In addition, the

This work was supported in part by the Shandong Provincial Natural Science Foundation under Grant ZR2020QE218 and in part by the National Natural Science Foundation of China under Grants 52122705. (Corresponding author: Hong Chen)

Hong Chen is with the School of Electrical Engineering and Automation, Shandong University of Science and Technology, Qingdao 266590, China (email: hongchen@sdust.edu.cn)

Dawei Li and Ronghai Qu are with the State Key Laboratory of Advanced Electromagnetic Engineering and Technology, School of Electrical and Electronic Engineering, Huazhong University of Science and Technology, Wuhan 430074, China. (e-mail: daweil@hust.edu.cn; ronghaiqu@mail.hust.edu.cn)

Tianjie Zou is with the Power Electronics, Machines and Control Group, University of Nottingham, Nottingham NG7 2 GT, U.K. (e-mail: tianjie.zou@nottingham.ac.uk).

FSPM machines have an essentially sinusoidal phase back-EMF, relatively high torque density, low torque ripple, and good flux-weakening capability [2]. Therefore, the FSPM machines have become attractive candidates for electrical vehicle propulsion, servo system, and wind power generation applications [3]-[5].

As a consequence, the FSPM machines have been extensively investigated, and various novel topologies are introduced and analyzed [6]-[19]. Based on stator structure, the FSPM machines can be divided into four groups, i.e., the U-core type [8]-[10], the multitooth type with the assisted tooth attached to each main tooth [11]-[13], the E-core type with alternative PM arrangement in the stator teeth [14]-[16], and C-core type with half number of stator teeth and PM poles compared to conventional U-core counterpart [17]-[19]. Among these, the U-core type was first proposed in 1997 [1], which has the advantages of a robust rotor and nonoverlapping windings, while they also suffer from limited electrical loading and high PM usage. Therefore, a multitooth FSPM machine was developed to reduce magnet usage [11]. Moreover, E-core and C-core FSPM machines were presented to further enlarge slot area and lower PM consumption, which achieve a higher torque density and simpler stator than those of the conventional counterpart [14], [17].

According to the operation principle of the FSPM machines, there are lots of feasible stator/rotor pole combinations [8], [17], which have significant influences on torque capacity and performance. To achieve high torque capacity, the optimal stator/rotor pole combination of the FSPM machine must be determined. However, the FSPM machines with different stator structures have various optimal pole combinations. As investigated, for the U-core FSPM machines, the optimized rotor pole number should be close to the stator pole number, and the classic combinations are 12/10 and 12/13 [10]. While for the multitooth FSPM machine, the 6/19 combination is a common selection [11]. Furthermore, for the E-core FSPM machines, it indicates in [12] that the optimal combinations should be that the rotor pole number is slightly smaller than twice the stator pole number, such as the 6/11 combination. Moreover, for the C-core FSPM machines, the 6/13 combination is reflected to exhibit relatively higher torque density [15].

However, most of the conclusions are based on finite-element analysis (FEA) comparisons, and difficult to use

the results for practical design, especially for novel FSPM topologies. Since there are barely any pieces of literature to provide a general method to get the optimal stator structure for FSPM machines with random rotor pole numbers, it brings computation burden and heavy workloads for designers and researchers to try and compare separately [9], [15]. To solve this problem, a mathematical method is needed to show the relationships between the torque capacity, the stator structure, and stator/rotor pole combinations. In previous research, though the traditional torque equations can be used to analyze the torque components conveniently from the perspective of the airgap field harmonics [18]-[20], it fails to show the relationships between torque capacity and stator structure clearly.

Therefore, this paper proposes a directional stator permeance design approach to achieve the maximum torque capacity under a given rotor, from a novel perspective of torque contributions by amplitudes and phase angles of the stator permeance harmonics. This article is organized as follows. The principle and flowchart of the directional stator design method are introduced in Section II. Then the torque contributions made by the stator permeance harmonics are calculated analytically, and the optimal strategy is presented in Section III. In Section IV, two FSPM machines with 6/19 and 6/13 combinations are taken as examples and optimized based on the proposed approach. Then in Section V, a prototype of a 6/19 FSPM machine is manufactured and measured to validate the analytical and FE analysis (FEA). Finally, some conclusions are drawn in Section VI.

II. DIRECTIONAL STATOR PERMEANCE DESIGN METHOD

From the view of stator permeance, different stator structures, including the conventional U-core type, C-core type, E-core type, and multitooth topologies can be expressed by a general analytical model. Thus, a C-core FSPM machine can be set as the primary topology, then other FSPM topologies with different stator types can be reflected by different values of permeance harmonics. In addition, a conventional rotor structure is applied in this general model. According to the simplified linear stator permeance model illustrated in Fig. 1, the stator permeance function $\Lambda_s(\theta)$ considering winding slots and PM slots [20] can be expressed by Fourier series:

$$\Lambda_s(\theta) = \Lambda_{s0} + \sum_m \Lambda_{sm} \cos(mZ_s\theta + \theta_{\Lambda m}) \quad (1)$$

where Λ_{s0} and Λ_{sm} are the amplitudes of the zeroth and m -th stator permeance harmonics, respectively, Z_s is the stator main tooth number, $\theta_{\Lambda m}$ is the phase angle of the m -th stator permeance harmonic and the value is 0 or π for each specific harmonic. Moreover, the phase angle for the zeroth harmonic is set to $\theta_{\Lambda 0}=0$.

Then the procedure of the directional tooth design approach is shown in Fig.2, which mainly consists of three steps.

Step I: Original Stator Permeance Investigation.

According to the initial parameters set on the FSPM machine, the original amplitude Λ_{sk} ($k=0,1,2,3,\dots$) and phase angle $\theta_{\Lambda k}$ of each stator permeance harmonic and corresponding torque

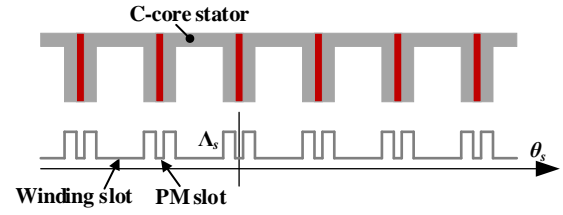


Fig. 1. Simplified stator permeance models of C-core FSPM machines.

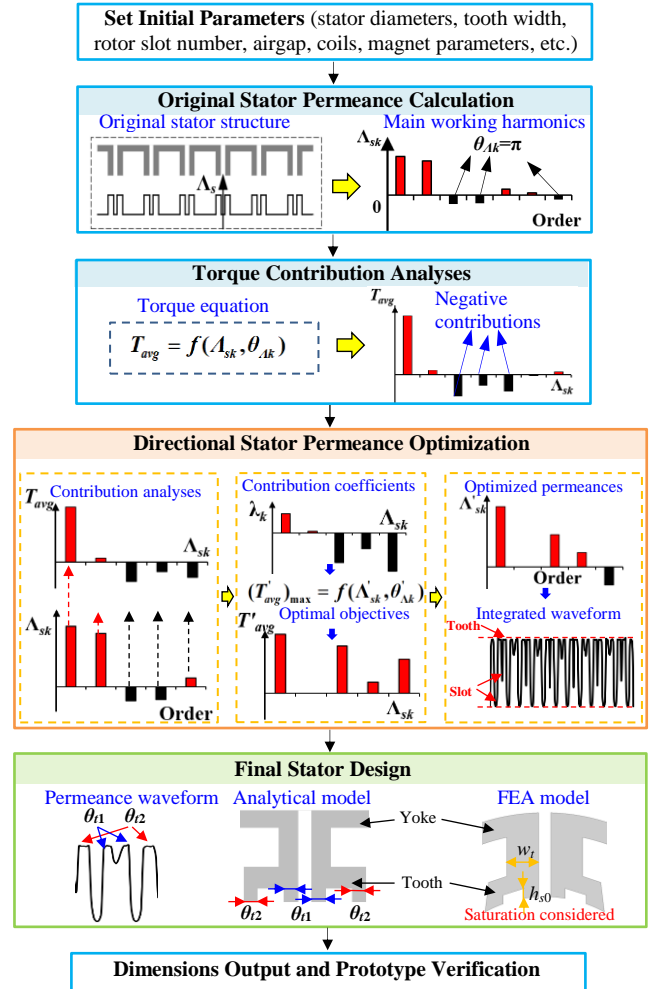


Fig. 2. Flowchart of the directional stator design method.

contribution can be obtained, based on a proposed analytical model.

Step II: Directional Permeance Harmonic Optimization.

To reveal the relationships between permeance harmonics and torque contributions, torque contribution coefficient λ_k is proposed, which is calculated as:

$$\lambda_k = \frac{T_{avgk}}{\Lambda_{sk}} \quad (2)$$

where T_{avgk} is the average torque produced by the k -th order permeance harmonic. The amplitude of the λ_k reflects the weight given to the corresponding harmonic. Thus, permeance harmonics with low weight should be reduced, considering the interaction between the harmonic amplitudes. Moreover, the positive/negative value of the λ_k means that the produced

torque increases/decreases the torque capacity. Based on the optimal strategy, optimized permeance harmonics with Λ'_{sk} and $\theta'_{\Lambda k}$ can be obtained.

Step III: Integrated Permeance Waveform.

Then synthesizing the stator permeance harmonics to get the integrated permeance waveform, which directly reveals the optimized stator tooth configuration with fuzzy dimensions. It should be noticed that the optimized amplitudes Λ'_{sk} and phase angles $\theta'_{\Lambda k}$ for the maximum torque may synthesize an improper shape or small slot area as a stator, and the values should be revised and checked again. Then, optimize the detail dimensions of the stator based on FEA, including the tooth width, slot area, slot height, etc.

Finally, the stator structure and dimensions of the FSPM machine can be obtained.

III. TORQUE CONTRIBUTION INVESTIGATION

A. Airgap Flux Density

The no-load airgap flux density $B_g(\theta, t)$ can be calculated as [19]

$$B_g(\theta, t) \approx \frac{g}{\mu_0} F_{pm}(\theta) \Lambda_s(\theta) \Lambda_r(\theta, t) \quad (3)$$

where $F_{pm}(\theta)$ is the MMF produced by PMs, $\Lambda_r(\theta, t)$ is the rotor permeance function with slotted rotor and slotless stator, g is the airgap length, and μ_0 is the vacuum permeability.

The expressions of $F_{pm}(\theta)$ and $\Lambda_r(\theta, t)$ can be given by (4) and (5) respectively,

$$F_{pm}(\theta) = \sum_{i=1,3,5,\dots} F_{pmi} \sin(i \frac{Z_s}{2} \theta) \quad (4)$$

$$\Lambda_r(\theta, t) = \Lambda_{r0} + \sum_n \Lambda_{rn} \cos[nZ_r(\theta - \Omega_r t - \theta_{r0})] \quad (5)$$

where F_{pmi} is the amplitude of the i -th harmonic of the PM MMF, Λ_{r0} and Λ_{rn} are the amplitudes of the zeroth and n -th rotor permeance harmonics, respectively, Ω_r is the mechanical angular velocity, and θ_{r0} is the initial angle.

Therefore, the no-load airgap flux density ignoring stationary harmonics can be obtained as

$$\begin{aligned} B_g(\theta, t) &= \frac{g}{\mu_0} F_{pm}(\theta) \Lambda_s(\theta) \Lambda_r(\theta, t) \\ &\approx \frac{g}{2\mu_0} \Lambda_{s0} \Lambda_{r1} \sum_i F_{pmi} \sin \left[\left(i \frac{Z_s}{2} \pm Z_r \right) \theta \right] \\ &\quad + \frac{g}{4\mu_0} \Lambda_{r1} \sum_i \sum_m \Lambda_{sm} F_{pmi} \sin \left[\left(i \frac{Z_s}{2} \pm Z_r \pm mZ_s \right) \theta \right] \end{aligned} \quad (6)$$

B. Torque Contribution Equation

Then the electromagnetic torque T_e of the FSPM machines can be calculated by

$$\begin{cases} T_e = \frac{e_A i_A + e_B i_B + e_C i_C}{\Omega_r} \\ e_q(t) = -\frac{1}{dt} r_g l_{st} \int_0^{2\pi} B_g(\theta, t) N_j(\theta) d\theta \end{cases} \quad (7)$$

where e_q ($q = A, B, C$) is the back-EMF of each phase, i_q is the

winding excitation, r_g is the airgap radius, l_{st} is the stack length, $N_j(\theta)$ is the winding function.

Then the average torque with $i_d=0$ can be expressed as:

$$\begin{aligned} T_{eavg} &= C_0 \Lambda_{s0} \sum_n \sum_i F_{pmi} K_{s0in} \Lambda_{rn} \\ &+ \frac{1}{2} C_0 \sum_n \sum_i \sum_m \Lambda_{sm} \Lambda_{rn} \cos(\theta_{\Lambda m}) F_{pmi} K_{smin} \quad (8) \\ &= \sum_k \lambda_k \Lambda_{sk} \end{aligned}$$

$$\text{where } K_{s0in} = \frac{k_w |i \frac{Z_s}{2} + nZ_r|}{i \frac{Z_s}{2} + nZ_r} - \frac{k_w |i \frac{Z_s}{2} - nZ_r|}{|i \frac{Z_s}{2} - nZ_r|} \quad (9)$$

$$\begin{aligned} K_{smin} &= \frac{k_w |i \frac{Z_s}{2} + nZ_r + mZ_s|}{i \frac{Z_s}{2} + nZ_r + mZ_s} - \frac{k_w |i \frac{Z_s}{2} - nZ_r - mZ_s|}{|i \frac{Z_s}{2} - nZ_r - mZ_s|} \\ &+ \frac{k_w |i \frac{Z_s}{2} + nZ_r - mZ_s|}{|i \frac{Z_s}{2} + nZ_r - mZ_s|} - \frac{k_w |i \frac{Z_s}{2} - nZ_r + mZ_s|}{|i \frac{Z_s}{2} - nZ_r + mZ_s|} \end{aligned} \quad (10)$$

, $C_0 = \frac{3}{2} \frac{g}{\mu_0} r_g l_{st} N_s Z_r I_m$, and N_s is the turns in series per phase, I_m is the amplitude of phase current, and k_{wv} is the winding factor of the v -th harmonic, i_d is the d -axis current, and λ_k is the contribution coefficients ($k=0,1,2,3,\dots$).

It can be observed that there are two components of the average torque, as listed in Table I. Under the condition of the same stator/rotor pole combination and volume limitation, it is reflected that Λ_{sk} and $\theta_{\Lambda k}$ directly determine the torque capacity. Moreover, according to (8), since the Λ_{sk} is positive, only the positive torque contribution coefficient λ_k can result in positive and useful torque components, which is directly related to the phase angle $\theta_{\Lambda k}$ and the positive/negative of the winding factor coefficient K_{ski} . In addition, the coefficients K_{s0i} and K_{smi} reflect the effects of the slot-pole combination and the winding configuration.

TABLE I
TORQUE CONTRIBUTIONS

Stator permeance	Torque contribution coefficient, λ_k	Flux density harmonic, v
Λ_{s0}	$C_0 \sum_n \sum_i F_{pmi} K_{s0in} \Lambda_{rn}$	$ i \frac{Z_s}{2} \pm nZ_r $
Λ_{sm}	$\frac{1}{2} C_0 \sum_n \sum_i \sum_m \Lambda_{rn} \cos(\theta_{\Lambda m}) F_{pmi} K_{smin}$	$ i \frac{Z_s}{2} \pm nZ_r \pm mZ_s $

C. Directional Stator Permeance Optimization

Since the torque contribution made by Λ_{s0} accounts for a relatively large proportion of the total average torque, to maximize the torque capacity, the m -th stator permeance harmonic with the optimized $\theta'_{\Lambda m}$ should generate the same torque polarity with that of the 0th order permeance harmonic. Hence, the optimal strategy of the phase angle $\theta'_{\Lambda m}$ can be obtained by

$$\theta'_{\Lambda m} = \begin{cases} \theta_{\Lambda m}, & T_{avg0} \cdot T_{avgm} > 0 \\ \theta_{\Lambda m} + \pi, & T_{avg0} \cdot T_{avgm} < 0 \end{cases} \quad (11)$$

where T_{avg0} and T_{avgm} are the original torque contributions of the 0th and m -th order harmonics. Therefore, when T_{avgm} and T_{avg0} are both positive or negative, the optimal phase angle $\theta'_{\Lambda m}$ is kept to be $\theta_{\Lambda m}$. On the contrary, $\theta'_{\Lambda m}$ should be inversed and become $(\theta_{\Lambda m} + \pi)$.

As for the optimal amplitude of the permeance harmonic Λ'_{sk} , it ranges from the minimum value $\Lambda_{s.min}$ to the maximum stator permeance $\Lambda_{s.max}$. In addition, the amplitudes Λ'_{sk} are also restricted mutually considering integration. As a result, the amplitudes of the optimal permeance harmonic Λ'_{sk} are constricted and determined by

$$\begin{cases} \Lambda_{s.min} \leq \Lambda'_{sk} \leq \Lambda_{s.max} \\ \Lambda_{s.min} \leq \Lambda'_{s0} + \sum_m \Lambda'_{sm} \cos(mZ_s\theta + \theta'_{\Lambda m}) \leq \Lambda_{s.max} \\ \Lambda_{s.max} = \frac{\mu_0}{g}, \quad \Lambda_{s.min} = \frac{\mu_0}{g + h_s} \end{cases} \quad (12)$$

where h_s is the slot depth.

Based on the above analyses, the objective function of the optimal stator permeance parameters is defined as

$$\begin{cases} \text{Function: } \max(T_{eavg}) \\ \text{Variables: } \Lambda_{sk}, \theta_{\Lambda m} \\ \text{Constraints: } T_{ripple} \% < 5\% \end{cases} \quad (13)$$

where $T_{ripple} \%$ is the ratio of the peak-peak torque ripple T_{ripple} to the average torque T_{eavg} , and the torque ripple T_{ripple} can be expressed as,

$$\begin{aligned} T_{ripple} = & C_0 \Lambda_{s0} \sum_{n=6k\pm 1} \sum_i n F_{pmi} K_{s0in} \Lambda_{rn} \\ & \times \cos[(n \mp 1)Z_r \Omega_r t + nZ_r \theta_0 \mp \theta_i] \\ & + \frac{1}{2} C_0 \sum_{n=6k\pm 1} \sum_i \sum_m n F_{pmi} \Lambda_{sm} \Lambda_{rn} K_{smin} \\ & \times \cos[(n \mp 1)Z_r \Omega_r t + nZ_r \theta_0 \mp \theta_i - \theta_{\Lambda m}] \end{aligned} \quad (14)$$

Then, by optimizing the amplitudes and phase angles of the stator permeance harmonics, an optimal stator structure can be obtained for the FSPM machine to achieve the maximum torque capacity. Importantly, it should be noted the proper slot area should be considered in the process of final result selection.

IV. OPTIMAL DESIGN AND PERFORMANCE ANALYSES

In this section, two FSPM machines with different rotor tooth numbers are designed and optimized based on the proposed directional stator optimization method.

A. Initial Design

According to the design procedure in Fig.2, the original stator structures of these two FSPM machines are set to be the C-core type, and the stator slot opening $b_{s0}=18\text{mm}$ is initially built, as illustrated in Fig.3(a) and (b). The main parameters are listed in Table II.

The non-overlapping windings are adopted, and the pole pair number is set to 2. Then the amplitudes and phase angles of the main stator permeance harmonics can be calculated and listed in Table III. Under the initial condition, the 0th~3rd stator

permeance harmonics feature relatively large amplitudes, while the 2nd, 3rd, and 6th harmonics have opposite phase angles compared to the other harmonics. Furthermore, the airgap flux density distributions are calculated and presented in Fig.4. It can be observed that the analytical results match well with the FEA results.

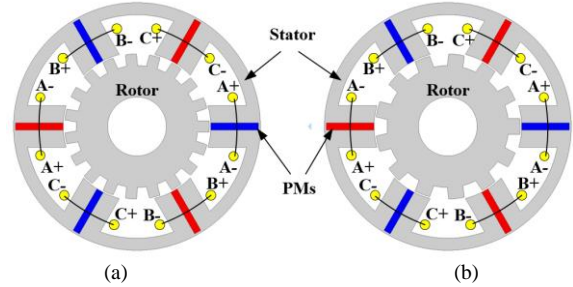


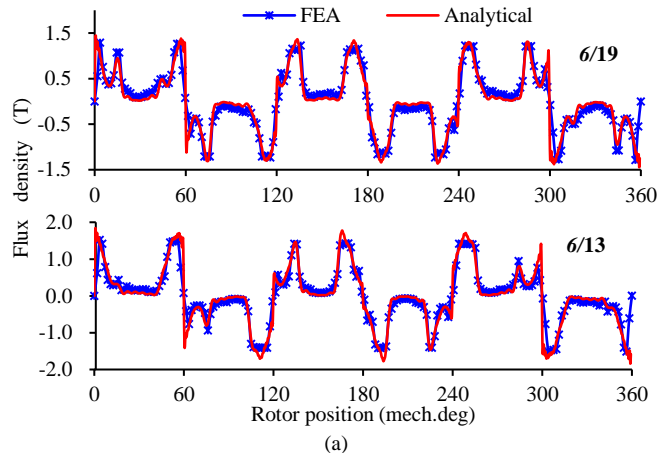
Fig. 3. Initial C-core FSPM machines. (a) 6/19 model. (b) 6/13 model.

TABLE II
MAIN PARAMETERS OF THE INITIAL FSPM MACHINES

Parameter	Unit	Value
Stator outer diameter	mm	126
Stator inner diameter	mm	75.4
Rotor tooth width	mm	5.6
Airgap length	mm	0.8
Magnet height	mm	3.6
Magnet width	mm	24
Stack length	mm	60
Slot area	mm ²	502
Magnet volume	cm ³	31.5
Turns in series per phase	-	200
Stator /rotor tooth number Z_s / Z_r	-	6/19 & 6/13
Rated rotational speed	rpm	600
Rotor slot opening/pitch	-	0.54
Magnet grade	-	N40SH
Steel material	-	35WW250

TABLE III
PARAMETERS OF THE ORIGINAL STATOR PERMEANCE HARMONICS

Permeance Harmonic order, k	Phase angle $\theta_{\Lambda k}$	Amplitude Λ_{sk} -FEA(Analytical) ($\times 10^{-3} \text{H/mm}^2$)
0	0	0.97 (0.94)
1	0	0.85 (0.89)
2	π	0.23 (0.20)
3	π	0.21 (0.23)
4	0	0.14 (0.15)
5	0	0.05 (0.08)
6	π	0.12 (0.12)



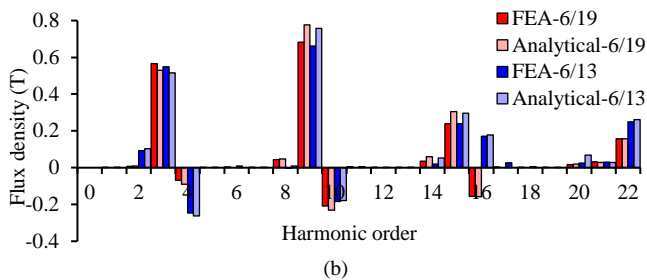


Fig. 4. Flux density distributions and harmonics comparison of the two FSPM machines. (a) Flux density waveforms. (b) Harmonics

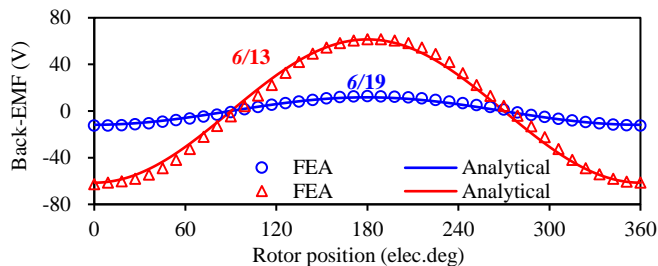


Fig. 5. Phase back-EMF waveforms at 600rpm.

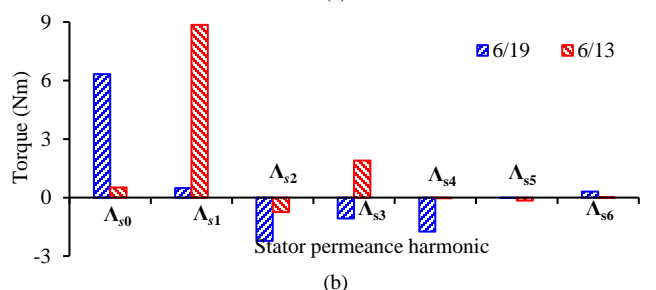
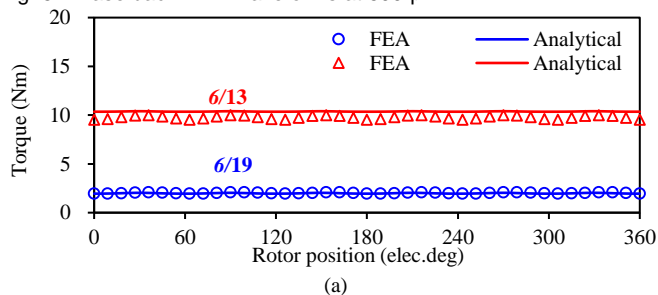


Fig. 6. Torque waveforms and contributions. (a) Torque waveforms. (b) Contributions

Moreover, the phase back-EMF and the electromagnetic torque waveforms are calculated based on (7), as presented in Fig.5 and Fig.6(a). It can be observed that the back-EMF and average torque of the 6/19 model are much lower than those of the 6/13 model. Thereinto, the amplitudes of the fundamental back-EMF are 12.6V and 62.8V, respectively, and the average torques are 2Nm and 9.8 Nm, respectively. The rated electric loadings are set to 253.3A/cm for these two FSPM machines.

It can be explained by the different contributions made by the stator permeance harmonics, as investigated in Fig.6(b). For the 6/19 model, the 0th permeance harmonic generates the largest share of the average torque. Moreover, the 0th, 1st, and 6th harmonics produce positive torque (7.1Nm), while the torque contributions made by the 2nd ~ 5th harmonics are negative (-5.0Nm). For the 6/13 model, the torque contribution by the 1st permeance harmonic is the maximum and up to 8.8 Nm. In

addition, only the 2nd harmonic contributes negative and low torque (-0.7Nm), and all the other harmonics produce positive contributions.

Thus, though the gear ratio (ratio of the rotor pole pair number to the pole pair number of armature winding) of the 6/19 model is larger than that of the 6/13 model, the torque density of the 6/19 model is much lower because of the negative torque contributions made by several permeance harmonics. What's more, it can be extensively applied to explain the same phenomenon in other flux modulation machines.

B. Stator Permeance Optimization

To obtain the maximum average torque and minimized torque ripple, the multi-objective genetic algorithm is adopted to optimize the main stator permeance parameters based on the directional permeance design method. According to the torque contribution investigation of the 6/19 model above, the contribution coefficients λ_k can be calculated and summarized in Table IV. Based on the directional permeance design method, the optimal phase angles $\theta'_{\Lambda k}$ of the permeance harmonics with negative λ_k (2nd ~ 5th orders) should be inverted to produce positive torque. Furthermore, the amplitude of each permeance harmonic should be optimized to maximize the torque capacity. As listed in Table IV, it can be observed that the λ_1 is only 0.09, which means that the 1st harmonic with a large amplitude produces rather low torque. Therefore, the optimal Λ'_{s1} should be decreased. Meanwhile, the harmonics with relatively higher λ_k , including the 2nd, 3rd, 4th, and 6th orders, should be enlarged. Since both the original amplitude Λ_{s5} and λ_5 are relatively low, it can be ignored to simplify the optimal process. As a result, the optimal amplitude ranges of the main permeance harmonics are set as listed in Table IV.

TABLE IV
OPTIMAL PERMEANCE PARAMETER OF THE 6/19 MODEL

Harmonic order, k	λ_k (p.u.)	Phase angle $\theta'_{\Lambda k}$	Ranges $\Lambda'_{sk}/\Lambda_{sk}$
0	1.00	0	[0.8, 1.3]
1	0.09	0	[0, 0.1]
2	-1.50	0	[0, 4]
3	-0.80	0	[0, 2]
4	-1.94	π	[0, 4]
5	-0.09	π	-
6	0.39	π	[0, 2]

With the constrictions and optimal function equations, the average torque (larger than 14.8Nm) and torque ripple of the cases with different Λ'_{sk} are scattered in Fig.7 (a). The red and green dots indicate the models with the maximum torque T_{max} and minimum torque T_{min} in the selected set. It can be seen that the maximum torque can reach to 18.1Nm. In addition, the torque ripple is much less compared to that of the original stator due to the reduced Λ'_{s1} . Then the integrated waveforms of the main stator permeance harmonics are illustrated in Fig.7(b). The directionally optimized permeance waveforms of both the T_{max} - and T_{min} -models reveal that the optimal stator structure for the 6/19 FSPM machine is the **multitooth type**. Accordingly, the amplitudes and phase angles of the T_{max} case and the original model are compared in Fig.7 (c). The sign(+/-) means

that each optimized permeance harmonic increases / decreases the total average torque. It can be seen that all the phase angles of the permeance harmonics contributing to negative torques are inversed. Therefore, most of the permeance harmonics will produce positive torque contributions and the torque capacity of the FSPM machine with the optimized stator can be significantly enlarged.

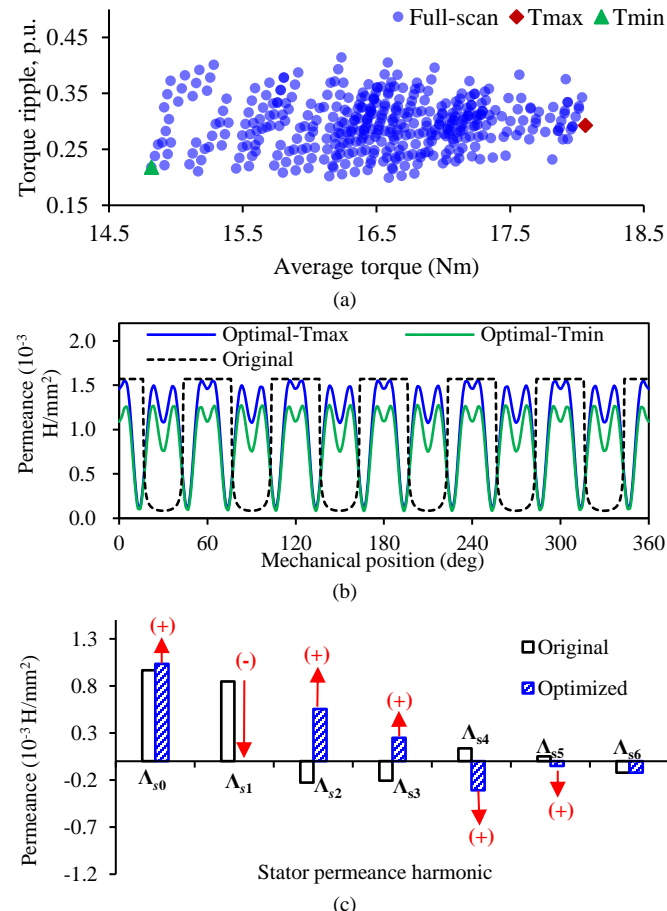


Fig. 7. Optimization results of the 6/19 FSPM machine. (a) Torque vs. torque ripple. (b) stator permeance waveforms. (c) Spectra.

TABLE V
OPTIMAL PERMEANCE PARAMETER OF THE 6/13 MODEL

Harmonic order, k	λ_k (p.u.)	Phase angle $\theta'_{\Lambda k}$	Ranges $\Lambda'_{sk}/\Lambda_{sk}$
0	0.05	0	[0.7, 1]
1	1.00	0	[1, 2]
2	-0.31	π	[0, 2]
3	0.89	π	[1, 2]
4	-0.02	π	[0, 2]
5	-0.28	π	[0, 2]
6	0.01	-	-

Likewise, the 6/13 model is optimized based on the directional permeance optimization, and the optimal ranges of the permeance parameters are set in Table V. Since the 1st order of the permeance harmonic produces the most torque, the contribution coefficients λ_k is set as the base. Though the 0th harmonic generates much less torque, the amplitude Λ'_{s0} should not be reduced a lot due to the constant airgap length. Consequently, the optimal ranges of the other harmonics are

smaller than that of the 6/19 model. Then Fig.8(a) shows the comparison of the optimized and the original permeance waveforms. It indicates that the variations of the optimal and original permeance are rather small, as compared to Fig.8(b). Therefore, it can be expected that the torque improvement is less than that of the 6/19 model.

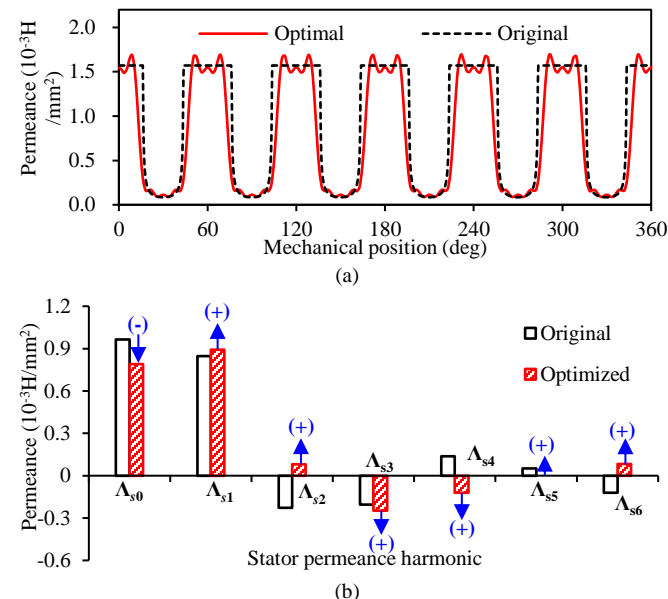


Fig. 8. Optimization results of the 6/13 FSPM machine. (a) stator permeance waveforms. (b) Spectra.

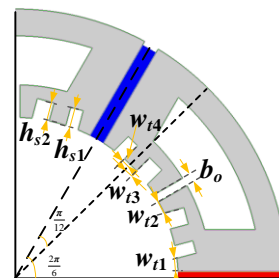


Fig. 9. The quarter cross-section of a 6-slot FSPM stator.

C. Sensitivity of Stator Tooth Dimensions

To gain the final stator structure from the stator permeance waveform, the relationships between the stator design parameters and the permeance harmonics should be further investigated. The main stator tooth parameters are depicted and labeled in Fig.9, including b_o , w_{t1} , w_{t2} , w_{t3} , w_{t4} , h_{s1} , and h_{s2} . Considering the symmetry and simplicity of the stator, the assisted tooth number is set to six. With the variations of the stator design parameters, the stator structure can be turned into the corresponding type.

Then a sensitivity analysis is proceeded to evaluate the influence of the stator design parameters on each permeance harmonic. Since the saturation effect of the FSPM machines with different stator types and slot-pole combinations are quite different, then the saturation impact on the stator permeance is ignored in the general analysis. Therefore, the sensitivity of the permeance harmonics can be calculated based on the DOE method and the Pearson correlation coefficient [21]-[22],

$$\rho(x_i, Y_i) = \frac{N \sum x_i Y_i - \sum x_i \sum Y_i}{\sqrt{N \sum x_i^2 - (\sum x_i)^2} \sqrt{N \sum Y_i^2 - (\sum Y_i)^2}} \quad (15)$$

where N is the sample number, x_i is the i -th design parameter, and Y_i is the optimization objective.

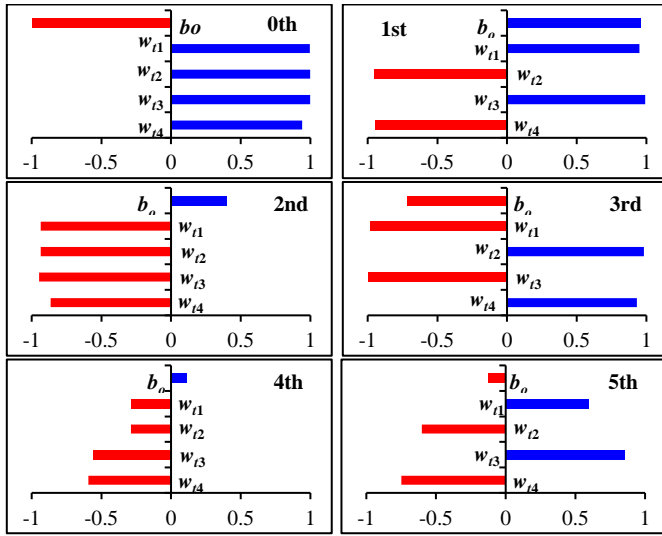


Fig. 10. Sensitivity of main stator design parameters with respect to permeance harmonic.

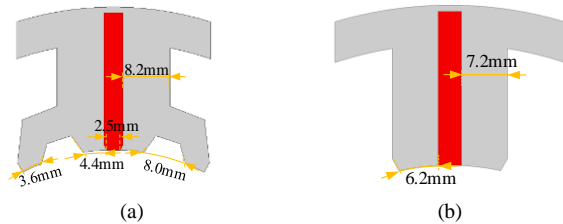


Fig. 11. Main stator dimensions of the optimized FSPM machines (a) 6/19 model. (b) 6/13 model.

Fig.10 shows the sensitivity of the stator tooth parameters with respect to permeance harmonics. The phase angle is considered in the value of each permeance as positive (0) or negative (π). The value of the 0th permeance harmonic increases as the b_o increases and assisted tooth widths decrease. Besides, the influences of the stator design parameters on the 2nd and 4th harmonics are rather similar, but contrary to that of the 0th harmonic. Likewise, the sensitivities of the design parameters concerning the 1st and 3rd harmonics are contrary. Except for the influence of the b_o , the sensitivity to the 5th harmonic is similar to that of the 1st harmonic. Furthermore, since saturation is not considered in this section, the sensitivities of h_{s1} and h_{s2} concerning each permeance harmonic are near zero, and not illustrated in Fig.10. As a result, the final 6/19 and 6/13 structures are presented in Fig.11 (a) and (b), respectively.

D. Performance Analysis

Fig.12 shows the back-EMF and torque comparisons of the optimized and initial FSPM machines with the 6/19 model. With the optimized stator permeance, the back-EMF of the optimized 6/19 model is largely increased compared to that of the initial waveforms predicted by FEA, as shown in Fig. 12 (a).

The RMS values predicted by FEA are 64.5V and 8.8V, respectively. Moreover, as calculated in Fig.12 (b), the average torque of the optimized 6/19 model based on the analytical method can be improved to 18.1 Nm, which matches well with the FEA results without considering core saturation. However, according to the flux density distribution of the 6/19 model under the rated load shown in Fig.13 (a), there is severe saturation in the stator. Therefore, the permeance harmonics are influenced by the saturation effect, as presented in Fig.12 (c). As a result, the average torque is adjusted to 12.3Nm based on FEA.

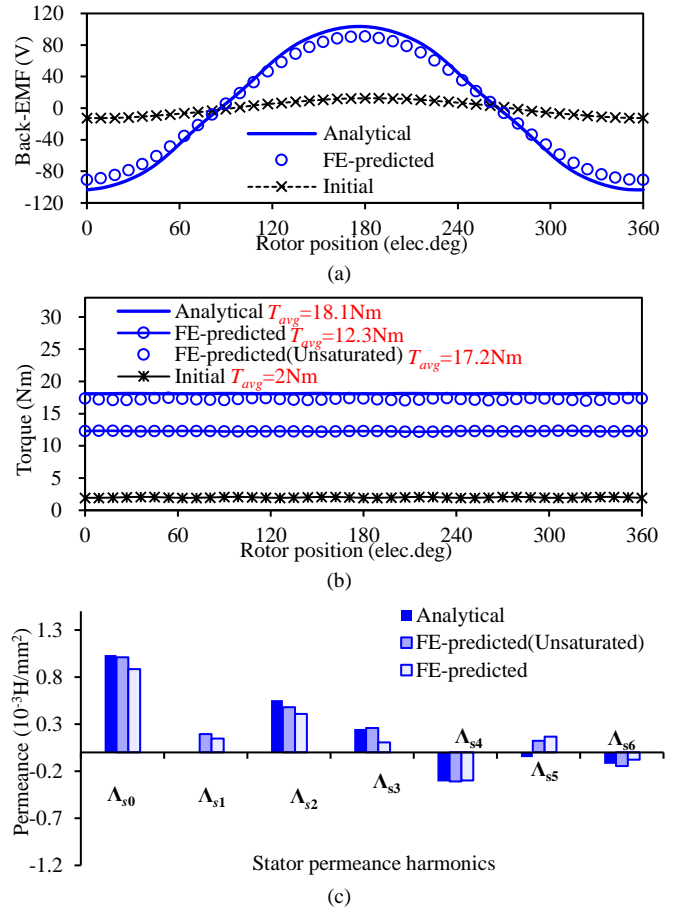


Fig. 12. Performances of the optimized 6/19 model. (a) Phase back-EMF. (b) Torque performance. (c) Permeance comparison.

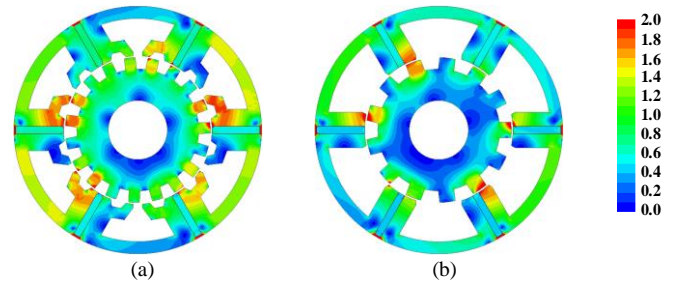


Fig. 13. Magnetic flux density distributions of the optimized FSPM machines under 253.3A/cm. (a) 6/19 model. (b) 6/13 model.

For the 6/13 FSPM machine, the back-EMF improvement is less significant than that of the 6/19 model, and the RMS values of the optimized and initial models are 49.4V and 44.5V,

respectively, as shown in Fig.14(a). Moreover, Fig.13 (b) reveals that the core saturation is less severe than that of the 6/19 model, and then the torque reduction because the saturation would be small. As compared in Fig.14 (b), the analytical result of the average torque with the optimized permeance can be improved to be 11.8Nm. Moreover, the average torque is adjusted to 10.9 Nm based on FEA, which is close to the analytical results.

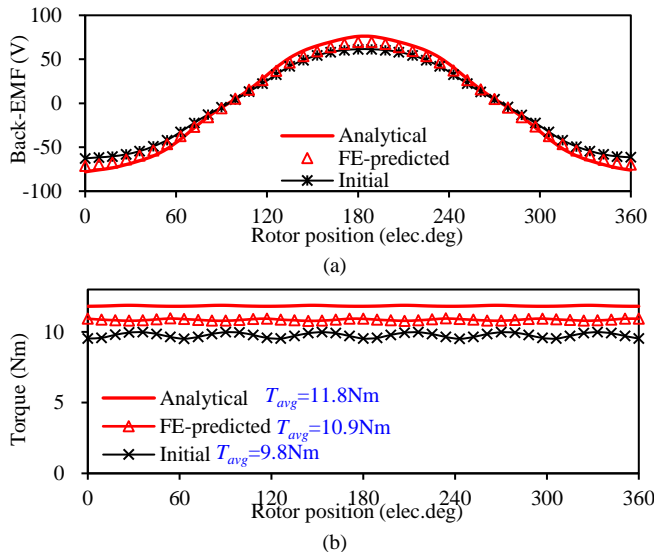


Fig. 14. Performances of the optimized 6/13 model. (a) Phase back-EMF. (b) Torque.

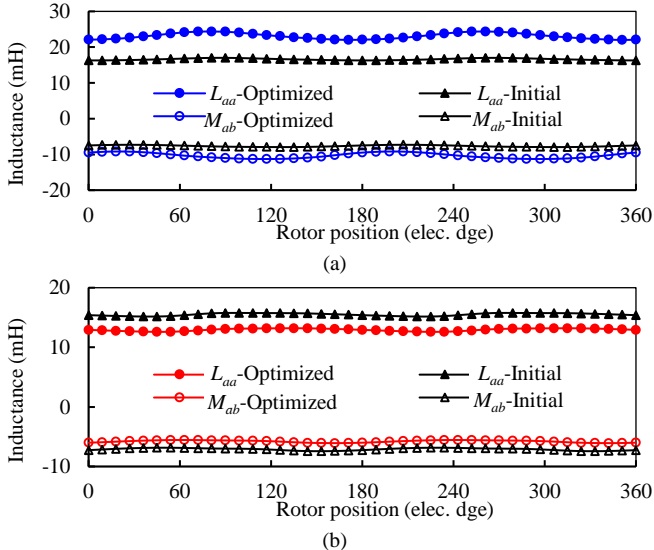


Fig. 15. Self- and mutual-inductances comparison in rated load condition. (a) 6/19 model. (b) 6/13 model.

Furthermore, the self- and mutual inductances of the 6/19 and 6/13 models are analyzed and compared in Fig.15, predicted by FEA. It can be observed that both the self- and mutual inductances of the optimized 6/19 model are enlarged, compared to that of the initial stator structure. Since the stator permeance harmonics have been optimized to maximize the average torque, the 2nd and 4th airgap flux density harmonics are increased, which results in inductance enlargement [23]. While for the 6/13 model, the inductances of the optimized

model are slightly lower than that of the initial model due to the smaller \$\Lambda_{s0}\$.

In addition, Fig.16 compares the FE-predicted power factor versus phase current curves of the 6/19 and 6/13 models. The power factor can be calculated by

$$PF = \frac{1}{\sqrt{1 + (\omega L_s I_q / E_q)^2}} \quad (16)$$

where \$\omega\$ is the electrical angular velocity, and \$L_s\$ is the synchronous inductance. Though the inductance of the optimized 6/19 model is enlarged, the back-EMF increases much more. Therefore, the power factor gets higher than that of the initial model. For the 6/13 model, the power factor of the optimized model is slightly higher than that of the initial model.

Moreover, the detailed electromagnetic performances of the initial and optimized FSPM machines with the same electrical loading are summarized in Table VI. It can be observed that the torque capacities of the FSPM machines with directionally optimized stator structures are improved effectively.

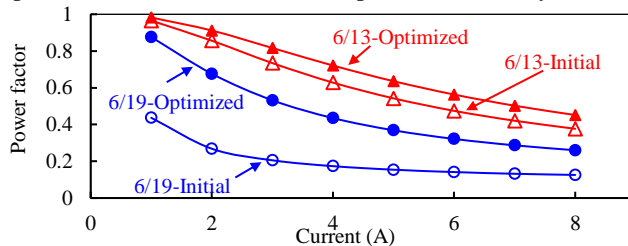


Fig. 16. Power factors of the FSPM machines with the 6/19 and 6/13 models.

TABLE VI
PERFORMANCE COMPARISON OF THE FSPM MACHINES
($I_{RMS}=5\text{A}$, SPEED=600RPM)

Parameter	6/19 model		6/13 model	
	Initial	Optimized	Initial	Optimized
Average torque (Nm)	2.0	12.3	9.8	10.9
Phase back-EMF (V)	8.8	64.5	44.5	49.4
Electrical loading (A/cm)	253.3	253.3	253.3	253.3
Copper loss @120°C (W)	77.1	90.5	77.1	70.5
Core loss (W)	8.6	18.7	6.3	6.0
PM loss (W)	4.9	6.83	2.2	1.9
Efficiency (%)	58.1	86.9	87.8	89.7
Self-inductance (mH)	16.6	23.1	15.5	12.9
Mutual inductance (mH)	-7.6	-10.4	-7.1	-5.8
Power factor	0.15	0.37	0.54	0.63

V. EXPERIMENTAL VALIDATION

To verify the foregoing analyses and prediction, a prototyped FSPM machine with a multitooth stator and 6/19 stator/rotor combination is manufactured and tested. The main parameters and materials are listed in Table VII. Fig.17 (a) presents photos of the main parts of the prototype, and the output torque is measured by the torque transducer, as shown in Fig.17 (b).

Fig.18 shows the measured and FE-predicted back-EMF waveforms and harmonic spectra at 600 rpm. It can be seen that the simulated and measured results match well, as shown in Fig.18(a). In addition, as analyzed in Fig.18 (b), the amplitudes of the fundamental components based on 3D-FEA are lower than the 2D-FEA results, due to the relatively small ratio of axial length to stator outer diameter (40mm/122.5mm), which results in a significant end-effect. While the measured result is

slightly lower than the 3D-FEA results, because of fabrication tolerances.

TABLE VII
KEY PARAMETERS OF THE PROTOTYPE

Parameter	Value	Parameter	Value
Stator outer diameter (mm)	122.5	Coil turns	100
Stator inner diameter (mm)	72	Slot area (mm ²)	410
Airgap length (mm)	0.8	Magnet height (mm)	3.6
Stack length (mm)	40	Magnet volume (cm ³)	20.9
PM material	40SH	Iron core material	30WW250
Rated speed (rpm)	600	Rated current (A)	5.0

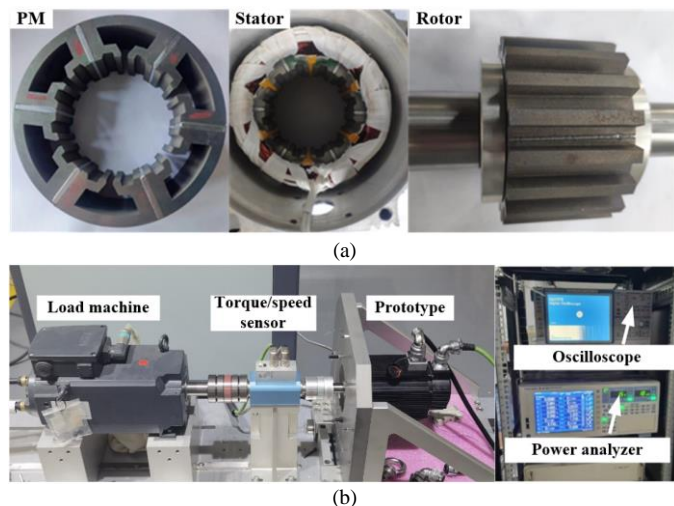


Fig. 17. Prototype of the optimized 6/19 FSPM machine. (a) Stator and rotor structures. (b) Test platform.

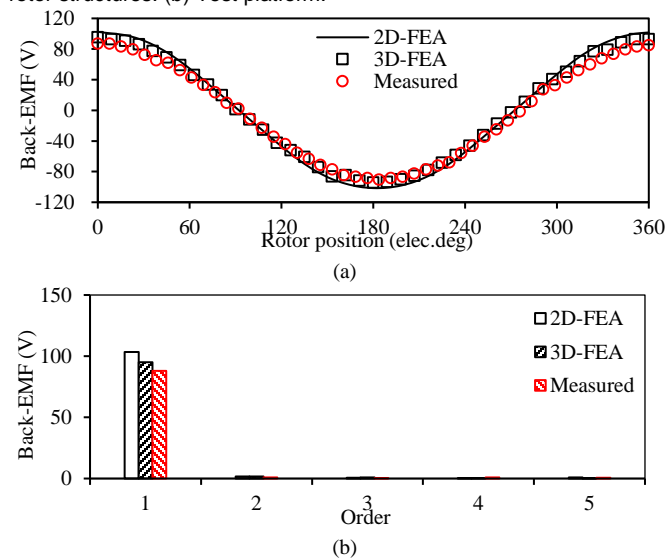


Fig. 18. Open-circuit line-line back-EMF comparison (at 600 rpm). (a) Waveforms. (b) Harmonics

The measured torque waveform is shown in Fig.19. Fig.20 presents the curves of the steady-state average torque versus phase current predicted by FEA and measured results. As can be seen, the difference gets larger with increasing loading due to the core saturation and increased magnet temperature. Furthermore, Fig.21 compares the curves of the efficiency versus different phase currents at the rated speed. Due to the effect of mechanical friction and simulation errors of core loss prediction, the measured efficiencies are lower than the

FE-predicted results. Overall, the tested and FE-predicted results are in good agreement, which can verify the correctness of the theoretical and simulated analyses.

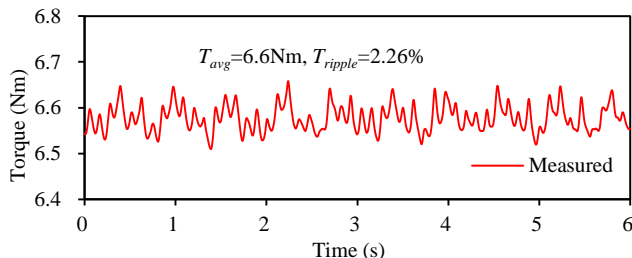


Fig. 19. Measured torque waveforms. ($I_{rated}=5\text{A}$).

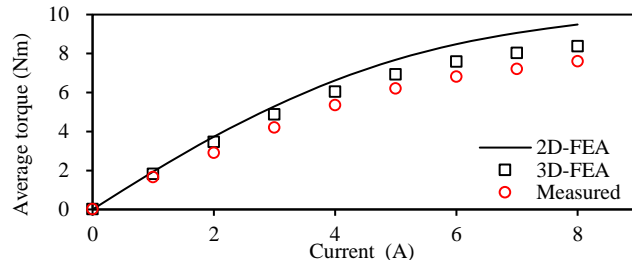


Fig. 20. Curves of steady-state average torque versus current ($I_{rated}=5\text{A}$).

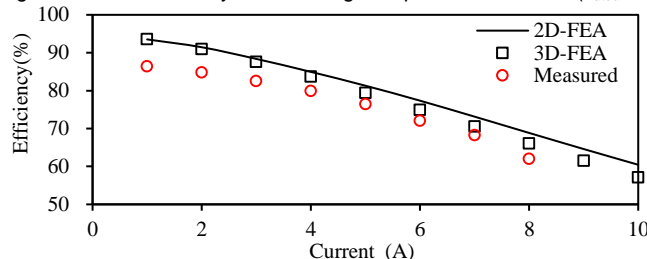


Fig. 21. Curves of efficiency versus phase current at 600rpm.

VI. CONCLUSION

In this article, a directional stator permeance design approach is proposed to maximize the torque capacity of the FSPM machines under a given rotor. To investigate relationships between the average torque and stator structures, the function of the torque and amplitudes and phase angles of the stator permeance harmonics $T_{eavg}=f(\Lambda_{sk}, \theta_{\Lambda k})$ is established. The main principle of the directional stator permeance design method is to make all the permeance harmonics with high torque contribution coefficients produce positive torque, and restrict the negative effects of other permeance harmonics by comprehensively designing the amplitudes and phase angles of the stator permeance harmonics. Based on the proposed design approach, two examples with different slot/pole combinations are designed and analyzed. Both the FEA and experimental results show that the proposed method can derive the optimal stator structures to maximize the torque capacities of the FSPM machines with the original rotor and winding configuration.

REFERENCES

- [1] E. Hoang, H. B. Ahmed, and J. Lucidarme, "Switching flux permanent magnet polyphased synchronous machines," in *Proc. Eur. Conf. Power Electron. Appl.*, 1997, pp. 903–908.
- [2] Z. Zhu, Y. Pang, D. Howe, S. Iwasaki, R. Deodhar, and A. Pride, "Analysis of electromagnetic performance of flux-switching permanent

- magnet machines by non-linear adaptive lumped parameter magnetic circuit model," *IEEE Trans. Magn.*, vol. 41, no. 11, pp. 4277–4287, Nov. 2005.
- [3] H. Chen, A. M. EL-Refaei, and N. A. O. Demerdash, "Flux-switching permanent magnet machines: A review of opportunities and challenges—Part I: Fundamentals and topologies," *IEEE Trans. Energy Convers.*, vol. 35, no. 2, pp. 684–698, Jun. 2020.
- [4] X. Zhu, Z. Shu, L. Quan, Z. Xiang, and X. Pan, "Design and multi-condition comparison of two outer-rotor flux-switching permanent-magnet motors for in-wheel traction applications," *IEEE Trans. Ind. Electron.*, vol. 64, no. 8, pp. 6137–6148, Aug. 2017.
- [5] L. Shao, W. Hua, N. Dai, M. Tong, and M. Cheng, "Mathematical modeling of a 12-phase flux-switching permanent-magnet machine for wind power generation," *IEEE Trans. Ind. Electron.*, vol. 63, no. 1, pp. 504–516, Jan. 2016.
- [6] M. Amirkhani, M. Kondelaji, A. Ghaffarpour, M. Mirsalim, and S. Vaez-Zadeh, "Study of Boosted Toothed Biased Flux Permanent Magnet Motors," *IEEE Trans. Trans. Electrific.*, vol. 8, no. 2, pp. 2549–2564, Jun. 2022.
- [7] F. Shen, J. Mei, H. Chen, Y. Zuo, S. Xie, and C. Lee, "Novel flux-switching machine with star-array permanent-magnet arrangement," *IEEE Trans. Ind. Electron.*, vol. 69, no. 9, pp. 8851–8861, Sep. 2022.
- [8] J. D. McFarland, T. M. Jahns, and A. M. El-Refaei, "Analysis of the torque production mechanism for flux-switching permanent-magnet machines," *IEEE Trans. Ind. Appl.*, vol. 51, no. 4, pp. 3041–3049, Jul./Aug. 2015.
- [9] Z. Z. Wu and Z. Q. Zhu, "Analysis of air-gap field modulation and magnetic gearing effects in switched flux permanent magnet machines," *IEEE Trans. Magn.*, vol. 51, no. 5, May 2015, Art. no. 8105012.
- [10] P. Wang, W. Hua, G. Zhang, B. Wang and M. Cheng, "Torque ripple suppression of flux-switching permanent magnet machine based on general Air-gap field modulation theory," *IEEE Trans. Ind. Electron.*, vol. 69, no. 12, pp. 12379–12389, Dec. 2022.
- [11] Z. Zhu, J. Chen, Y. Pang, D. Howe, S. Iwasaki, and R. Deodhar, "Analysis of a novel multi-tooth flux-switching PM brushless AC machine for high torque direct-drive applications," *IEEE Trans. Magn.*, vol. 44, no. 11, pp. 4313–4316, Nov. 2008.
- [12] J. T. Chen, Z. Q. Zhu, and D. Howe, "Stator and rotor pole combinations for multi-tooth flux-switching permanent-magnet brushless AC machines," *IEEE Trans. Magn.*, vol. 44, no. 12, pp. 4659–4667, Dec. 2008.
- [13] G. Zhao, Z. Li, W. Hua, X. Jiang, and P. Su, "Comparative study of winding configuration on a multitooth flux-switching permanent magnet machine," *IEEE Trans. Magn.*, vol. 58, no. 2, No. 8100405, Feb. 2022.
- [14] J. Chen, Z. Zhu, S. Iwasaki, and R. P. Deodhar, "A novel E-core switched flux PM brushless AC machine," *IEEE Trans. Ind. Appl.*, vol. 47, no. 3, pp. 1273–1282, May/Jun. 2011.
- [15] J. Zhu, L. Wu, and H. Wen, "Optimization and comparison of dual-armature flux-switching permanent magnet machines with different stator core shapes," *IEEE Trans. Ind. Appl.*, vol. 58, no. 1, pp. 314–324, Jan./Feb. 2022.
- [16] W. Ullah, F. Khan, E. Sulaiman, M. Umair, N. Ullah, and B. Khan, "Analytical validation of novel consequent pole E-core stator permanent magnet flux switching machine," *IET Electr. Power Appl.*, vol. 14, no. 5, pp. 789–796, May 2020.
- [17] J. Chen, Z. Zhu, S. Iwasaki, and R. Deodhar, "Influence of slot opening on optimal stator and rotor pole combination and electromagnetic performance of switched-flux PM brushless AC machines," *IEEE Trans. Ind. Appl.*, vol. 47, no. 4, pp. 1681–1691, Jul./Aug. 2011.
- [18] H. Yang, Y. Li, H. Lin, Z. Zhu, and S. Lyu, "Principle investigation and performance comparison of consequent-pole switched flux PM machines," *IEEE Trans. Trans. Electrific.*, vol. 7, no. 2, pp. 766–778, Jun. 2021.
- [19] D. Li, R. Qu, J. Li, W. Xu, and L. Wu, "Synthesis of flux switching permanent magnet machines," *IEEE Trans. Energy Convers.*, vol. 31, no. 1, pp. 106–117, Mar. 2016.
- [20] P. Wang, W. Hua, G. Zhang, B. Wang, and M. Cheng, "Principle of flux-switching PM machine by magnetic field modulation theory—Part I: Back-EMF generation," *IEEE Trans. Ind. Electron.*, vol. 69, no. 3, pp. 2370–2379, Mar. 2021.
- [21] L. Xu, W. Wu, W. Zhao, G. Liu, and S. Niu, "Robust design and optimization for a permanent magnet vernier machine with hybrid stator," *IEEE Trans. Energy Convers.*, vol. 35, no. 4, pp. 2086–2094, Dec. 2020.
- [22] X. Zhu, Z. Xiang, L. Quan, W. Wu and Y. Du, "Multimode optimization design methodology for a flux-controllable stator permanent magnet

memory motor considering driving cycles", *IEEE Trans. Ind. Electron.*, vol. 65, no. 7, pp. 5353–5366, Jul. 2018.

- [23] P. Wang, W. Hua, G. Zhang, B. Wang, and M. Cheng, "Inductance characteristics of flux-switching permanent magnet machine based on general air-gap filed modulation theory," *IEEE Trans. Ind. Electron.*, vol. 69, no. 12, pp. 12270–12280, Dec. 2022.



Hong Chen (Member, IEEE) was born in Shandong, China. She received the B. E.E. degree from the Wuhan University of Science and Technology, Wuhan, China, in 2010, and the Ph.D. degree from the Huazhong University of Science and Technology, Wuhan, China, in 2015, both in electrical engineering.

She is currently a Lecturer with the School of Electrical Engineering and Automation, Shandong University of Science and Technology. Her research interests include the design of permanent magnet machines and special electrical machines.



Dawei Li (Senior Member, IEEE) was born in Henan, China. He received his B.E.E. degree from the Harbin Institute of Technology, Harbin, China, in 2010 and his Ph.D. degree from the Huazhong University of Science and Technology, Wuhan, China, in 2015, both in electrical engineering.

In 2015, he joined the Huazhong University of Science & Technology. He has authored more than 60 published technical papers and is the holder of more than 10 patents/patent applications. His research interests include the design and analysis of flux-modulation permanent-magnet brushless machines.

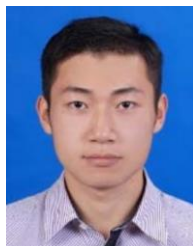
Dr. Li received the 2016 Best Poster Presentation Award from the XXIIth International Conference on Electrical Machines (2016) and Hubei Province Excellent Doctoral Dissertation (2016), China.



Ronghai Qu (Fellow, IEEE) received his B.E.E. and M.S.E.E. degrees in electrical engineering from Tsinghua University, Beijing, China, and the Ph. D degree in electrical engineering from the University of Wisconsin-Madison, Madison, WI, USA, in 1992, 1996 and 2002, respectively.

Since 2010, he has been a professor with the School of Electrical and Electronic Engineering, Huazhong University of Science and Technology, Wuhan, China. He has authored more than 230 published technical papers and is the holder of more than 50 patents/patent applications.

Dr. Qu is a Full Member of Sigma Xi. He was the recipient of several awards from the GE Global Research Center since 2003, including the Technical Achievement and Management Awards. He was also the recipient of the 2003 and 2005 Best Paper Awards, third prize, from the Electric Machines Committee of the IEEE Industry Applications Society (IAS) at the 2002 and 2004 IAS Annual Meetings, respectively.



Tianjie Zou (Member, IEEE) was born in Hubei, China. He received a B.E.E degree in electrical and electronic engineering and the Ph.D. degree in electrical engineering from the Huazhong University of Science and Technology, Wuhan, China, in 2013 and 2018, respectively.

He joined the Power Electronics, Machines and Control (PEMC) Group, University of Nottingham, Nottingham, U.K., in 2018, as a Research Fellow. His main research interests include the design, analysis, and intelligent control of electric machines, with special attention paid to advanced winding-integration technology in high-speed, high-power permanent magnet (PM) machines for electrified transportation.